Progress in Organic Coatings 177 (2023) 107427

Contents lists available at ScienceDirect

Progress in Organic Coatings

journal homepage: www.elsevier.com/locate/porgcoat

Poly-lactic acid coatings on the biomedical WE43 Mg alloy: Protection mechanism and ion permeation effects

Jianwei Dai [a,b], Changqing Wu [a,b], Juyi Yang [a,b], Lu Zhang [a,b], Qiangsheng Dong [a,b], Linyuan Han [a,b], Xuan Li [a,b], Jing Bai [a,b], Feng Xue [a,b], Paul K. Chu [c], Chenglin Chu [a,b,*]

[a] School of Materials Science and Engineering, Southeast University, Nanjing 211189, China
[b] Jiangsu Key Laboratory for Advanced Metallic Materials, Southeast University, Nanjing 211189, China
[c] Department of Physics, Department of Materials Science and Engineering, and Department of Biomedical Engineering, City University of Hong Kong, Hong Kong, China

ARTICLE INFO

Keywords:
Ion permeation
Poly-lactic acid coating
Magnesium alloy
Degradation behavior
Corrosion

ABSTRACT

Poly-lactic acid (PLA) coatings are deposited on the biomedical WE43 Mg alloy and the degradation behavior and mechanism are investigated during 504 h immersion in Hanks' solution. The protection mechanism is investigated by studying the ion permeation phenomenon and a custom *in situ* apparatus is constructed to evaluate the performance and elucidate the underlying principle. Na^+ and Cl^- penetrate the PLA membrane gradually and the different permeation effects stem from the different hydrated radii. Ion permeation can be separated into three stages. Penetration of Cl^- is dominant in the first stage and Na^+ dominates in the third stage. Penetration of Ca^{2+}, PO_4^{3-} along with other ions also take part in the third stage leading to the formation of Ca–P on the WE43 substrate. Based on the experimental results, models are established to describe the ion permeation behavior through the PLA membrane and predict the protection efficiency of the PLA coating. The results enrich our understanding of ion permeation in polymeric coatings and provide insights into the development of Mg-based biomedical implants.

1. Introduction

Biodegradable implants are becoming more important in the treatment of bone fractures and vascular injuries since they degrade spontaneously during tissue healing consequently obviating the need for a second surgery and mitigating the trauma and economic burdens of patients. Magnesium (Mg) and its alloys are attractive biodegradable biometals boasting excellent biocompatibility, mechanical properties, and natural biodegradation [1–6]. For example, the WE43 Mg alloy has been used in bone fracture implants due to the proper mechanical and degradation properties [7–9]. In order to overcome the main drawbacks caused by fast and nonuniform corrosion, protective polymeric coatings have been deposited on the Mg alloy to improve the properties [10–13]. For instance, Poly-lactic acid (PLA) coatings have received extensive attentions for their unique biodegradability, semi-crystallinity and excellent processability as compared to other polymeric coatings [14]. In general, PLA coatings can retard the corrosion of Mg alloys [15–17], control the alkaline microenvironment at the interface [18–20], and deliver therapeutic drugs [21,22]. However, there are still many questions concerning the protection efficiency and mechanism of PLA coatings.

It has been reported that PLA coatings improve the initial corrosion resistance [15,23–26] and the effectiveness increases with coating thickness [27]. However, in the physiological environment, the corrosion protection rendered by PLA coatings deteriorates with time [18,27] and coating delamination has been observed in some cases. In general, ion permeation plays an important role in the corrosion mechanism of coated metals. Coatings (usually nondegradable) act as the barrier to retard penetration of aggressive ions from the external medium to mitigate corrosion of the substrate. Slower permeation of cations also minimizes debonding of coatings. However, different from permanent (nondegradable) coatings, the micropores in PLA coatings are convenient channels for ion permeation. In addition, the degradation of PLA and Mg influence ion penetration dynamically and different ions in the external environment complicate the phenomenon. Another issue is how the protection efficiency changes with time. Previous studies have mainly focused on weight losses or electrochemical tests. However, changes in the local microenvironment at the interface are also crucial to

* Corresponding author at: School of Materials Science and Engineering, Southeast University, Nanjing 211189, China.
E-mail address: clchu@seu.edu.cn (C. Chu).

https://doi.org/10.1016/j.porgcoat.2023.107427
Received 4 November 2022; Received in revised form 29 December 2022; Accepted 11 January 2023

attaining a better understanding of the overall mechanism [20,28–30]. Recently, some studies have addressed the interface microenvironment by theoretical means [23,31,32], but *in-situ* quantitative investigations are expected to provide more accurate information about the changes in the protection efficacy with time.

Another important issue is the effectiveness of coatings as drug carriers and delivery agents. Since protection depends on ion permeation, it is time dependent and the durability and stability of coatings are critical, especially when drugs are stored for controlled and timely release. It is known that different ions cause different effects. For example, the permeation of chloride ions (Cl^-) can be mitigated by carboxyl and acidic sulfonic acid functional groups which have selective permeability to cations in the early stage [33,34]. Dong et al. [35] have studied the properties of epoxy resin coatings in the KCl solution and noticed that Cl^- is preferentially transported in the coatings compared to potassium ions (K^+). Therefore, it is important to perform a comprehensive study and compare the permeation behavior of anions and cations.

In this work, an *in-situ* custom apparatus is constructed to investigate the protection mechanism of PLA coatings on the WE43 Mg alloy. Penetration of the main cation and anion (Na^+ and Cl^-) is studied by immersion tests in Hanks' solution. Based on the experimental results, the ion permeation behavior through the PLA membrane is discussed and its influence on the degradation of the WE43 alloy is investigated. Models are established to describe and predict the ion permeation behavior through the PLA coating.

2. Materials and methods

2.1. Materials preparation

The composition of the commercial WE43 Mg alloy determined by inductively-coupled plasma atomic emission spectroscopy (ICP-AES) is listed in Table 1. An electrical discharge machine was used to prepare the disks with dimensions of Φ 50 × 2 mm. The WE43 alloy samples were ground progressively with silicon carbide sandpaper up to 2000# grit, ultrasonically cleaned in ethanol for 10 min, and dried by warm air. The PLA granules (4032D, Nature Works LLC, USA) were dried in an oven and then 0.5 g of PLA was dissolved in 5 mL of dichloromethane (CH_2Cl_2). After magnetic stirring for 24 h at room temperature, the solution was poured into a glass petri dish and dried naturally in air. The thickness of PLA membrane was measured by the screw micrometer caliper at ten different locations to ensure reliability. Herein, the PLA membrane had a diameter of 60 mm and the thickness of 0.10 ± 0.02 mm.

2.2. In vitro degradation

In vitro degradation was monitored at 37.5 ± 0.5 °C using the *in-situ* custom experimental setup consisting of the chamber and multi-channel ionometer based on the STM32 microcontroller, as shown in Fig. 1. The PLA membrane and WE43 alloy specimen were placed in the middle and side of the chamber. The medium (Hanks' solution, Table 2) and deionized water (DI water) were placed on both sides of the PLA membrane as illustrated in Fig. 1(b). In Hanks' solution, Na^+ and Cl^- are the main cation and anion. The Na^+ and Cl^- concentrations and pH were monitored everyday by the multi-channel ionometer. After 24 h, the Na^+ and Cl^- concentrations and pH hardly changed regardless of the position of the ion electrode and therefore, three ion electrodes were used as shown in Fig. 1(b).

2.3. Electrochemical evaluation

Electrochemical impedance spectroscopy (EIS) was conducted on an electrochemical workstation (Ametek PARSTAT 3000A-DX) based on the standard three electrode configuration. Two platinum flakes with an exposed area of 1 cm^2 were the working electrode (Pt_2) and counter electrode (Pt_1), respectively, and the saturated calomel electrode (SCE_1) was the reference electrode, as marked by WE1, CE1 and RE1 respectively in Fig. 1(b). EIS was performed on the PLA membrane from 10 kHz to 100 mHz with a sinusoidal perturbation of 10 mV. The electrochemical tests of the WE43 alloy were carried out using the three-electrode setup with the WE43 disk with an exposed surface of Φ 30 mm being the working electrode, saturated calomel electrode (SCE_2) as the reference electrode, and platinum flake (Pt_2) as the counter electrode, which were labeled as WE2, RE2 and CE2. EIS was conducted in the frequency ranging from 100 kHz to 100 mHz with a perturbing signal of 10 mV. The EIS data were analyzed with the aid of suitable equivalent circuit models by the ZSimpWin 3.60 software.

2.4. Characterization

After degradation, the PLA membrane was rinsed with DI water and dried in an oven. The corroded WE43 alloy was cleaned in a boiling CrO_3 (200 g/L) solution to remove the corrosion products. The surface morphology of the degraded PLA membrane and WE43 alloy was observed by scanning electron microscopy (SEM, FEI Sirion 200) and elemental composition was determined by energy-dispersive X-ray spectroscopy (EDS, Oxford Aztec X-Max 80). Fourier transform infrared spectroscopy (FTIR) was performed on the pristine and degraded PLA membranes (Thermo Scientific, Nicolet iS10) using the attenuated total reflection (ATR) mode from 4000 cm^{-1} to 500 cm^{-1} by averaging 16 scans with a resolution of 4 cm^{-1}. Tetrahydrofuran (THF) (4 mL:20 mg ratio) was used to dissolve the PLA membrane fragments. The number-average molecular weight (M_n) and weight-average of molecular weight (M_w) of the polymer were determined by gel permeation chromatography (GPC, Agilent PL-GPC 220) using polystyrene as the reference and THF as the eluent.

The thermal properties of the PLA membrane before and after degradation were determined by differential scanning calorimetry (DSC, PerkinElmer DSC8000) in nitrogen at a heating rate of 5 °C/min from ambient temperature to 200 °C. The melting temperature (T_m), and melting enthalpy (ΔH_m) were derived from the DSC curves and the crystallinity (χ_c) was calculated by the following equation:

$$\chi_c = \frac{\Delta H_m}{\Delta H_m^0} \times 100\%. \quad (1)$$

where χ_c is the crystallinity degree, ΔH_m is the experimental melting enthalpy obtained from the DSC data, and ΔH_m^0 is the melting enthalpy of 100% PLA (93.6 J/g) [36].

3. Results

3.1. Changes of Na^+ and Cl^- concentrations

Figs. 2(a) and (b) show the changes of the Na^+ and Cl^- concentrations in DI water *versus* immersion time. The Na^+ concentration is stable in the first 348 h before increasing from 0.61 mmol/L to 12.02 mmol/L thereafter. In comparison, the Cl^- concentration changes slightly in the first 108 h and then also increases abruptly. When immersion exceeds

Table 1
Elemental composition (*wt%*) of the WE43 alloy determined by ICP-AES.

	Mg	Y	Nd	Gd	Zn	Zr	Ni	Fe	Cu
WE43	Bal.	4.50	2.09	1.17	0.21	0.39	0.001	0.001	0.013

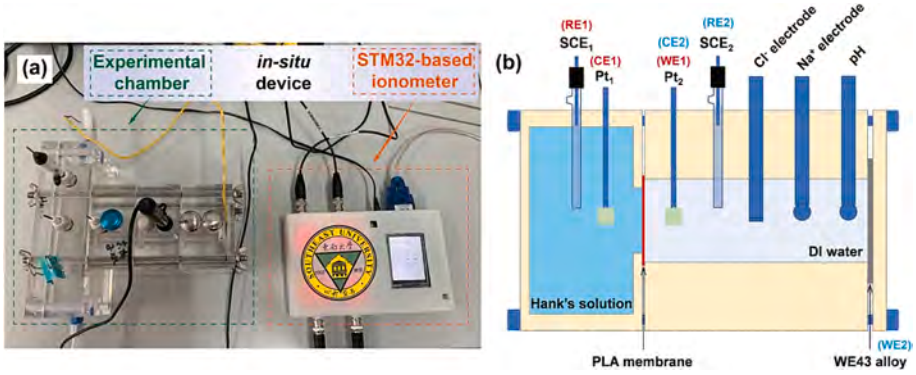

Fig. 1. (a) Custom apparatus for assessing ion permeation and (b) Schematic diagram of the experimental setup.

Table 2
Ion concentrations in Hanks' solution.

Ions	Na^+	Cl^-	K^+	Mg^{2+}	Ca^{2+}	HCO_3^-	HPO_4^{2-}	SO_4^{2-}
Concentration (mmol/L)	141.8	145.0	5.8	0.8	1.3	4.1	0.3	0.8

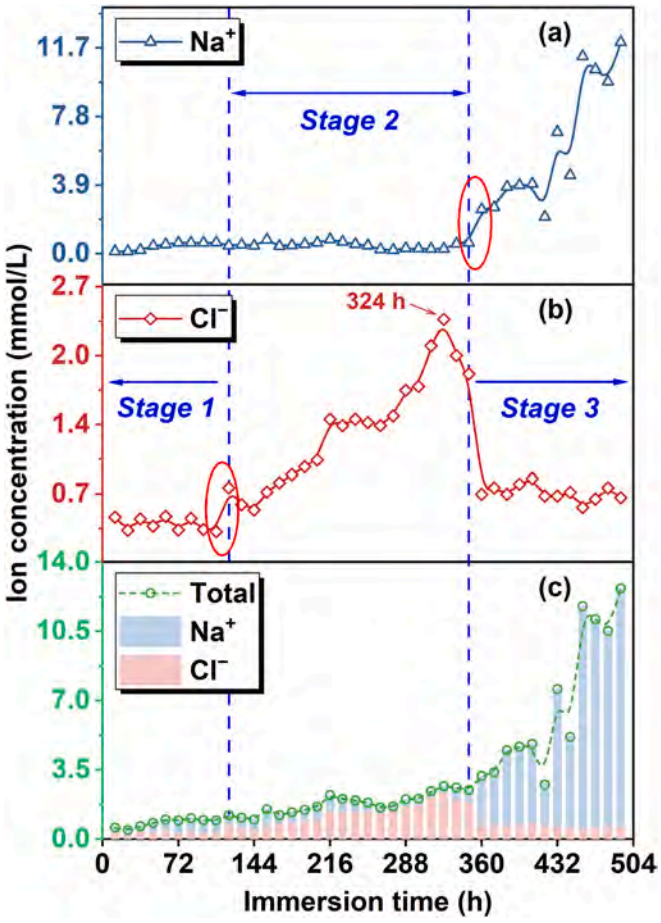

Fig. 2. Changes of (a) Na^+ and (b) Cl^- concentrations and (c) Total concentration of Na^+ and Cl^- *versus* immersion time.

324 h, the Cl^- concentration decreases remarkably and then stabilized as shown in Fig. 2. The relationship between the total concentration of Na^+ and Cl^- and immersion time is presented in Fig. 2(c), which reveals that the total concentration increases gradually with degradation time. Cl^- appears to play a dominant role in the first 348 h, but the role of Na^+ becomes more obvious during prolonged immersion. According to the experimental results acquired after 108 h and 348 h, the degradation process can be divided into three stages. As shown in Fig. 3, the pH of DI water increases initially from 8.84 to 9.94 and then decreases gradually after 396 h. This corresponds to when the Cl^- concentration decreases.

3.2. Electrochemical properties of the PLA membrane

The EIS results are presented in Fig. 4. After immersion for 324 h immersion, the EIS spectra of the PLA membrane appear corresponding to stage 3 in the ion concentration curve, when the total concentration of Na^+ and Cl^- increases dramatically. As shown in Fig. 4(a), the Nyquist plots almost overlap and can be approximated as straight lines. The frequency-phase Bode plots show that the phase angles in the low frequency region are larger. The equivalent circuit model is displayed in Fig. 4(b) in which R_s is the solution resistance, CPE_{PLA} and R_{PLA} are the constant phase element and resistance related to the PLA membrane, respectively. The curves after immersion for 324 h, 456 h, 480 h, and 504 h can be fitted by the same equivalent circuit $R_s(CPE_{PLA}R_{PLA})$, whereas the rest of the results are fitted by R_sCPE_{PLA}. CPE has been reported to be linear in the limited frequency range [37,38] and the fitting

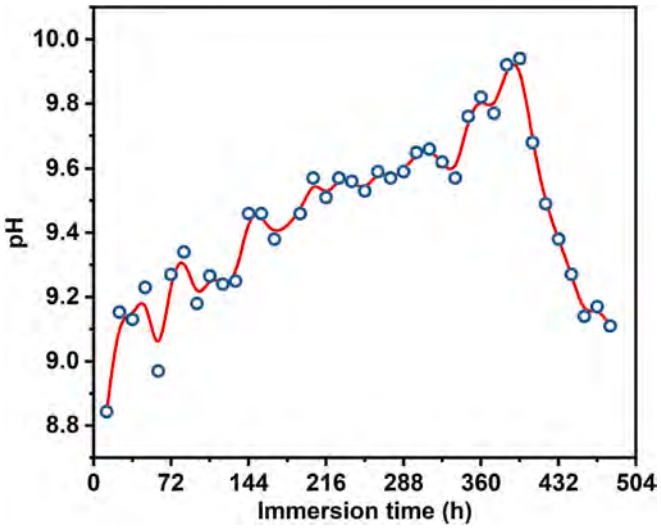

Fig. 3. pH *versus* immersion time during degradation.

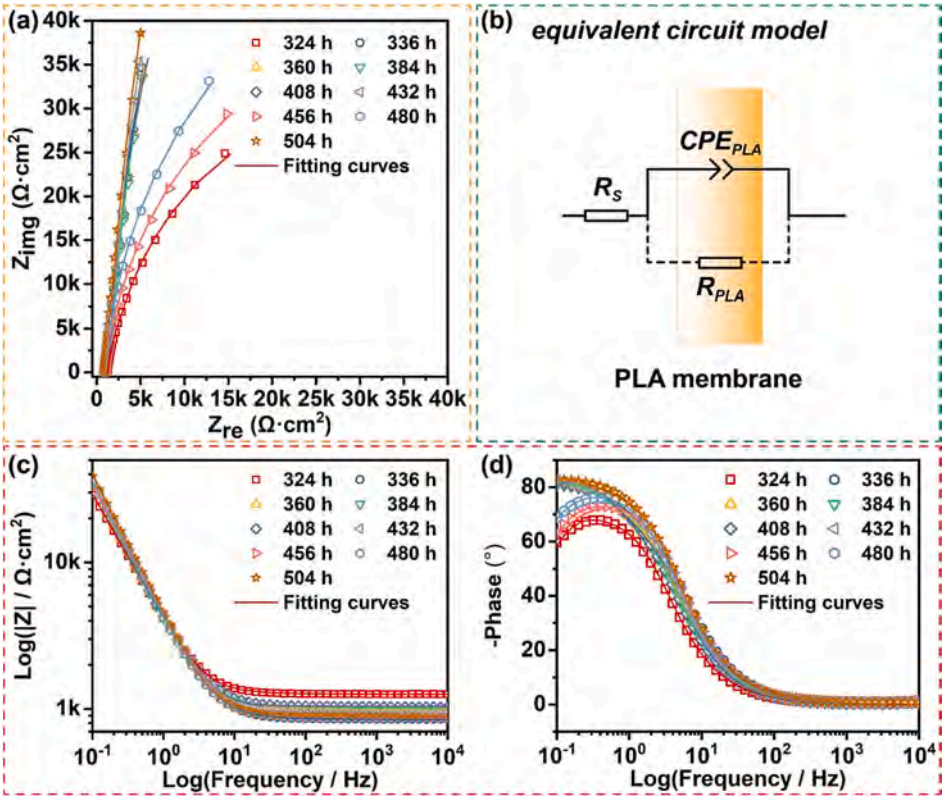

Fig. 4. EIS results of the PLA membrane: (a) Nyquist plots, (b) Equivalent circuit model, (c) Frequency-|Z| Bode plots, and (d) Frequency-phase Bode plots.

parameters are listed in Table 3. As immersion proceeds, Y decreases slightly and the fitted R_{PLA} increases gradually.

3.3. Electrochemical properties of the WE43 Mg alloy

The EIS results of the WE43 alloy without the PLA membrane are shown in Fig. 5. The Nyquist plots show a semi-circular arc, indicating that an electric double layer is formed at the interface between the Mg alloy and DI water. The frequency-phase Bode plots in Fig. 5(d) show only one peak suggesting one time constant in the corrosion process. The equivalent circuit $R_{s\text{-}DI}(CPE_{dl}R_{ct})$ is used to fit the EIS results as shown in Fig. 5(b), in which $R_{s\text{-}DI}$ is the resistance of DI water and R_{ct} and CPE_{dl} represent the charge transfer resistance and electric double-layer capacity, respectively. The effective capacitance ($C_{eff,\ dl}$) represented by CPE_{dl} is evaluated by Brug's formula [39] as shown in Eq. (2):

$$C_{eff,\ dl} = Y_{dl}^{\frac{1}{n}} \times \left(\frac{1}{R_s} + \frac{1}{R_{ct}}\right)^{\frac{n-1}{n}}. \quad (2)$$

Table 3
Fitted parameters obtained from the EIS measurement of the PLA membrane in Fig. 4.

Degradation time (h)	R_s ($\Omega\cdot cm^2$)	CPE_{PLA}		R_{PLA} ($\times 10^4$ $\Omega\cdot cm^2$)	χ^2 ($\times 10^{-5}$)
		Y ($\mu\Omega^{-1}\cdot cm^{-2}s^n$)	n		
324	1258.0	48.3	0.920	7.5	5.2
336	848.5	45.4	0.924	–	2.9
360	995.2	45.5	0.923	–	3.3
384	1019.0	46.5	0.923	–	6.1
408	1032.0	44.7	0.927	–	4.5
432	979.1	43.8	0.929	–	5.9
456	879.3	42.9	0.940	9.2	5.7
480	888.7	42.0	0.955	12.6	5.3
504	889.2	39.8	0.952	114.2	5.9

The fitted parameters are listed in Table 4. The DI water resistance $R_{s\text{-}DI}$ decreases gradually and R_{ct} increases as corrosion proceeds. The relationship between the R_{ct} and immersion time is displayed in Fig. 6. According to the stages presented in Fig. 2, the variation of R_{ct} can also be divided into three stages. In the early stage of degradation (0−120 h), R_{ct} goes up significantly. As corrosion proceeds (120–216 h), R_{ct} decreases indicative of decreased corrosion resistance of the WE43 alloy. In the third stage (216–348 h), R_{ct} increases. It can be inferred that a dense corrosion product layer is formed on the WE43 alloy in Stage 2 to retard corrosion resistance. In the last stage (348–504 h), R_{ct} increases slightly.

3.4. Structure and surface morphology of the PLA membrane

FTIR spectra are acquired from the PLA membrane before and after degradation as shown in Figs. 7(a) and 7(b). The peaks at 2997 and 2946 cm^{-1} are the stretching mode of -CH_3 band and that at 1453 cm^{-1} represents asymmetric bending of -CH_3. The peaks at 1180 and 1079 cm^{-1} are associated with stretching of -CO and that at 1360 cm^{-1} represents the vibration of -CH. The PLA membrane after degradation shows a wide band between 3050 and 3700 cm^{-1} which can be assigned to -OH stretching. A larger absorption band is observed at 1644 cm^{-1} derived from -OH bending. The chemical structure changes as a result of the hydrolysis of the PLA membrane. Additionally, the intensity of the peak for stretching of C=O at 1747 cm^{-1} changes slightly compared to the pristine PLA membrane because water breaks the ester bond. The peak at 2922 cm^{-1} represents symmetric stretching of -CH_2 and that at 2849 cm^{-1} corresponds to stretching of -CH and both become weaker after immersion for 504 h. The peak at 824 cm^{-1} represents CO_3^{2-} from corrosion products on the PLA membrane.

The DSC curves of the PLA membrane before and after degradation are displayed in Fig. 7(c). The melting temperature (T_m) decreases slightly from 169.6 ± 1.5 °C to 168.6 ± 1.3 °C, indicating degradation of the PLA membrane. The melting enthalpy (ΔH_m) before degradation is

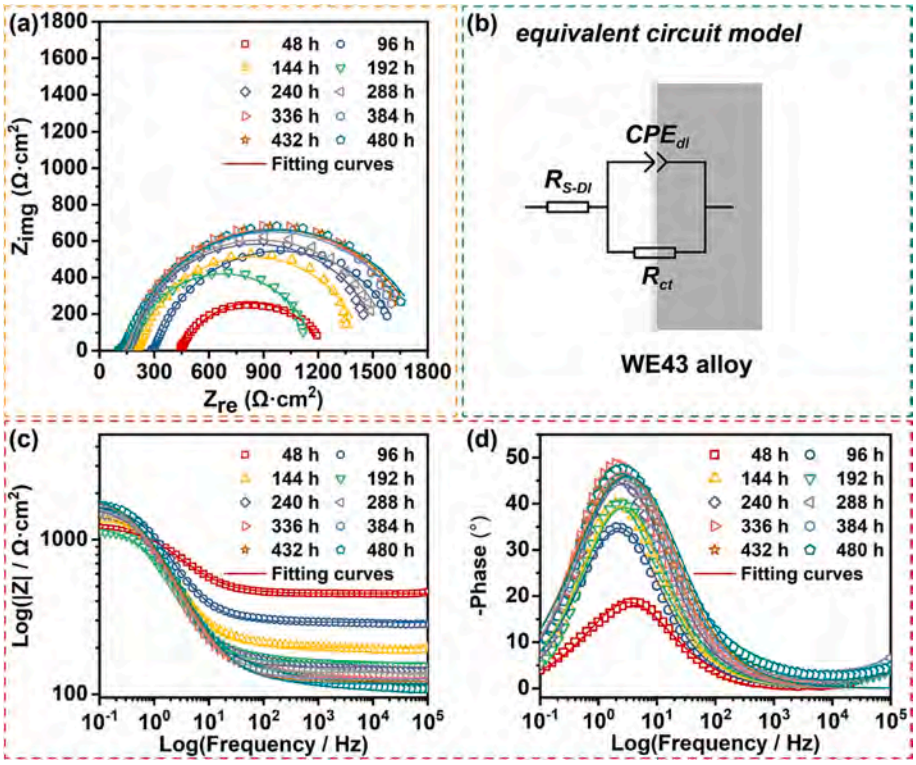

Fig. 5. EIS results of the WE43 alloy in DI water with ions that permeated through the PLA membrane: (a) Nyquist plots, (b) Equivalent circuit model, (c) Frequency-|Z| Bode plots, and (d) Frequency-phase Bode plots.

Table 4
Fitted parameters based on EIS measurement of the WE43 alloy in Fig. 5.

Degradation time (h)	$R_{s\text{-}DI}$ ($\Omega\cdot cm^2$)	CPE_{dl}		R_{ct} ($\Omega\cdot cm^2$)	$C_{eff,\ dl}$ ($\times 10^{-5}$ F·cm^{-2})	χ^2 ($\times 10^{-4}$)
		Y_{dl} ($\mu\Omega^{-1}\cdot cm^{-2}s^n$)	n			
48	446.3	222.0	0.743	785.5	8.6	4.8
96	292.1	191.4	0.820	1426.0	9.7	8.4
144	200.5	210.1	0.835	1299.0	10.9	2.1
192	159.7	245.3	0.826	1069.0	12.1	2.0
240	149.1	221.6	0.827	1490.0	10.7	3.1
288	138.1	222.8	0.819	1527.0	10.1	3.6
336	127.6	228.2	0.811	1751.0	9.8	4.1
384	124.9	225.7	0.792	1768.0	8.7	4.0
432	120.8	224.5	0.784	1819.0	8.2	4.1
480	116.7	216.7	0.776	1848.0	7.4	4.0

30.0 ± 0.4 J/g and increases to 32.3 ± 0.7 J/g after degradation. The GPC curves of the PLA membrane before and after degradation are presented in Fig. 7(d). The differential distribution curve shifts gradually to the left after degradation indicating the breakage of ester bonds and macromolecular chains in the PLA membrane. According to Eq. (1), χ_c is 32.1 ± 0.4% and 34.4 ± 0.8% for the PLA membrane before and after degradation, respectively. As shown in Table 5, M_n and M_w decrease and the polydispersity index (*PDI*) increases from 1.91 to 2.11 after degradation indicative of more pronounced scission in the PLA membrane.

The SEM images of the PLA membrane before and after degradation are depicted in Fig. 8. The PLA membrane is prepared by solvent evaporation and hence, both the porous and dense surfaces are observed. The porous surface is smooth with some interconnected micropores as shown in Fig. 8(a). On the other hand, the dense surface shows small protrusions but no obvious micropores are detected. During immersion, the porous surface and dense surface are in contact with Hanks' solution and DI water, respectively, as shown in Fig. 1. The PLA membrane swells and the porous surface becomes smoother. Meanwhile, small particles are dispersed on the porous surface of the PLA membrane and deposits are formed in the vicinity of the pores as revealed by Fig. 8(c). The dense surface in contact with DI water also undergoes hydrolysis to produce small holes. In addition, localized cavities are detected and the porosity and fragment exfoliation increase, consequently decreasing the permeation resistance against water molecules and hydrated ions.

The SEM images and EDS elemental maps of the porous and dense surfaces after degradation are depicted in Fig. 9. After 504 h, the porous surface shows the presence of C, O, Na, Cl, Mg, and K. The small white particles on the porous surface are mainly magnesium salts and sodium salts and potassium salts were mainly embedded in the micropores. The same elements are detected from the dense surface, proving that Na^+, Cl^- and K^+ penetrate the PLA membrane. Additionally, Mg^{2+} created from corrosion of the WE43 alloy diffuses and adsorbs to the dense surface of the PLA membrane as shown in Fig. 9(b6). In general, both Na and Cl are dispersed in the vicinity of the micropores in the dense surface after 504 h. The Na, Cl, and K distributions on the dense surface are slightly different from those on the porous surface, maybe attributable to the difference in the absorption mechanism in the different

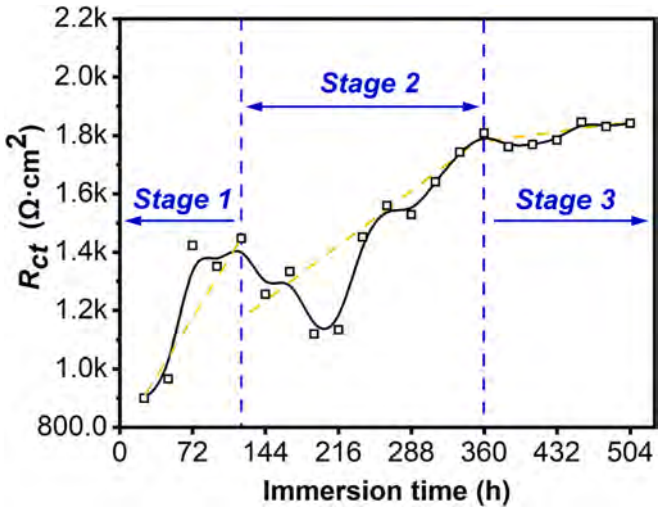

Fig. 6. R_{ct} *versus* immersion time during degradation of the WE43 alloy.

environments.

3.5. Surface morphology of the WE43 alloy

Fig. 10 shows the surface morphology of the WE43 alloy after degradation. The loose corrosion products are evenly distributed on the surface as shown in Figs. 10(a) and 10(b). After removing the corrosion products, corrosion pits are observed. According to the ion concentrations and the EIS spectra, the corrosion pits may be generated in Stage 2. Since Cl^- plays a dominant role in the ion permeation behavior through the PLA membrane, it may react with loose and porous $Mg(OH)_2$ to form soluble $MgCl_2$ and then the inner corrosion product layer is then destroyed during immersion. The chemical compositions of selected regions determined by EDS are shown in Fig. 10(d). C, O, and Mg are the main elements in the corrosion product layer with Mg to O being close to 1: 2 or 1: 3 indicative of $Mg(OH)_2$ or $MgCO_3$. It is noted that Cl is also detected from the corrosion product layer.

The cross-sectional image and EDS maps of the corroded WE43 alloy are displayed in Fig. 11. It is found that the uniform corrosion mode predominates for the WE43 specimen. The corrosion product layer with a thickness of 181.4 ± 19.3 μm is observed from the surface of the WE43 alloy. The inner layer is composed of mainly Mg and O and a Ca-containing layer with a thickness of 28.6 ± 0.5 μm is observed from the outer corrosion product suggesting permeation of Ca^{2+} in the later stage of degradation.

4. Discussion

4.1. Protection mechanism of the coating

Owing to the degradation of PLA and Mg, the corrosion behavior of the PLA-coated Mg alloy is complicated [15,18,23–27]. In order to clarify the mechanism, an *in-situ* apparatus is designed. The interface between the PLA coating and WE43 alloy is simulated by placing the PLA membrane and WE43 alloy in the middle and side of the chamber as illustrated in Fig. 1. In the simulated environment, the ester groups in PLA are susceptible to hydrolytic degradation in the presence of water as shown by the following reaction [4,28]:

Table 5
DSC and GPC parameters of the PLA membrane before and after degradation.

	T_m (°C)	ΔH_m (J/g)	χ_c (%)	M (g/mol)		*PDI*
				M_n	M_w	
Before degradation	169.6 ± 1.5	30.0 ± 0.4	32.1 ± 0.4	85,880	163,628	1.91
After degradation	168.6 ± 1.3	32.3 ± 0.7	34.4 ± 0.8	71,531	150,650	2.11

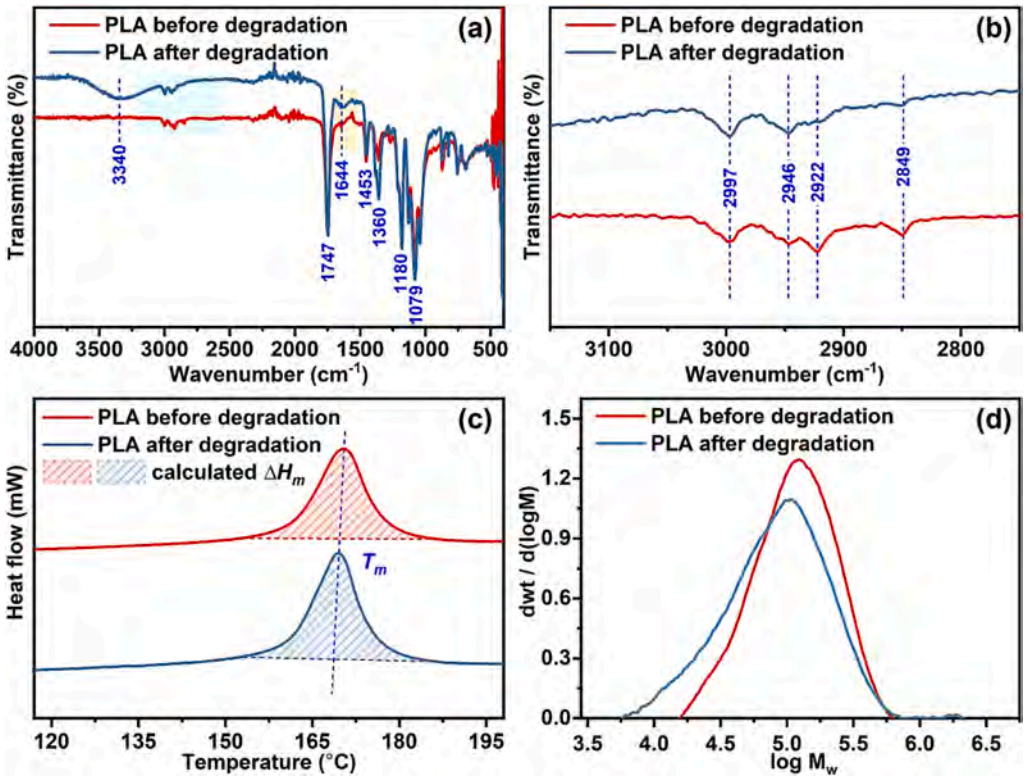

Fig. 7. (a) FTIR spectra and (b) Enlarged spectra of the selected region; (c) DSC curves; (d) GPC curves of the PLA membrane before and after degradation for 504 h.

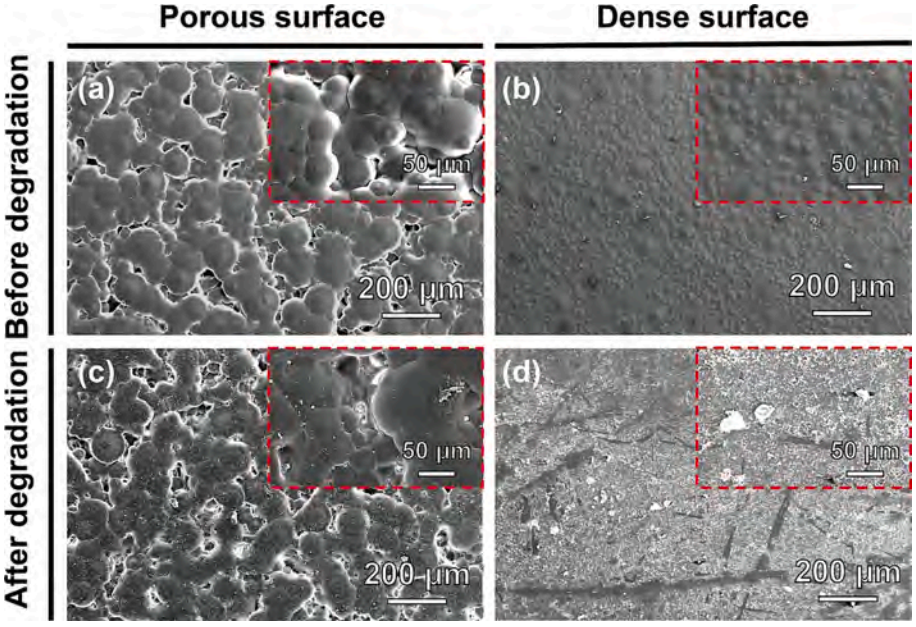

Fig. 8. SEM images of different regions of the PLA membrane before and after 504 h degradation: (a, c) Porous surface, (b, d) Dense surface; (a, b) Before degradation and (c, d) After degradation.

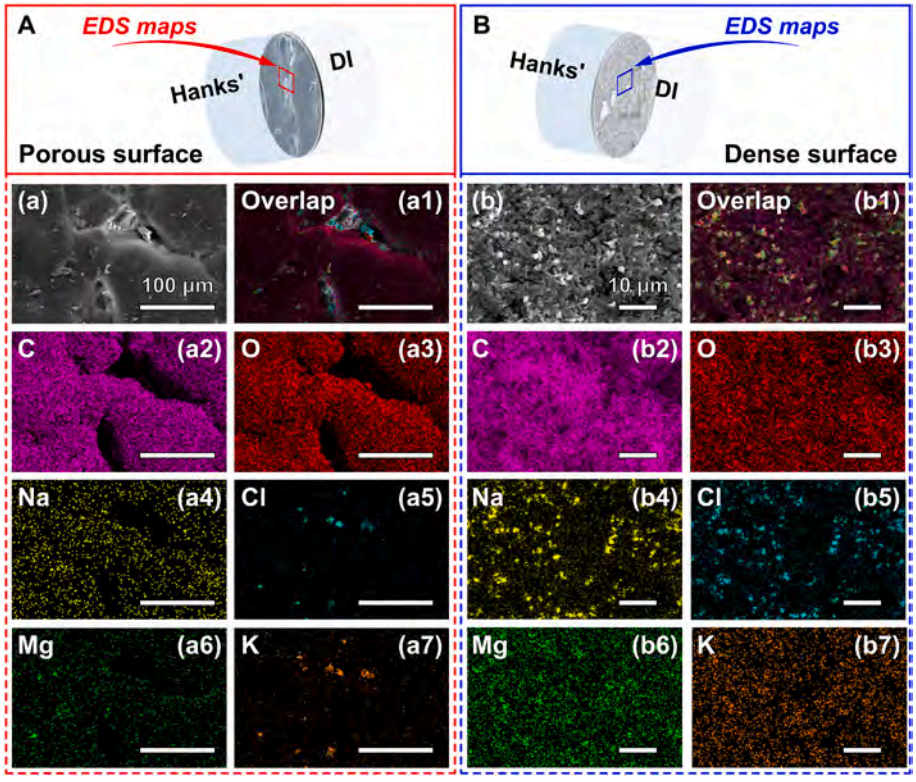

Fig. 9. Schematic diagrams of (A) Porous surface and (B) Dense surface of the PLA membrane together with SEM images and EDS elemental maps: (a) SEM image and (a1)-(a7) EDS elemental maps of the porous surface; (b) SEM image and (b1)-(b7) EDS elemental maps of the dense surface.

$$-COO + H_2O \rightarrow -OH + -COOH. \quad (3)$$

After degradation, the melting point of the PLA membrane decreases and the crystallinity increases slightly. GPC indicates that M_n of the PLA membrane changes from 85,880 g/mol to 71,531 g/mol corresponding to a decrease of 16.7%. In addition, *PDI* increases gradually from 1.91 to 2.11, indicating enhanced and random fragmentation of the molecular chains in the PLA membrane. According to DSC and GPC, the semi-crystalline PLA membrane undergoes hydrolysis and during immersion, degradation of PLA begins simultaneously in both the crystalline and amorphous regions [40]. The molecular chains in the amorphous region may degrade faster and so the crystallinity increases after degradation. The FTIR peaks of -OH and C═O are stronger after degradation as shown in Fig. 7(a), implying that the amounts of hydrophilic terminal -COOH and -OH groups increase. Therefore,

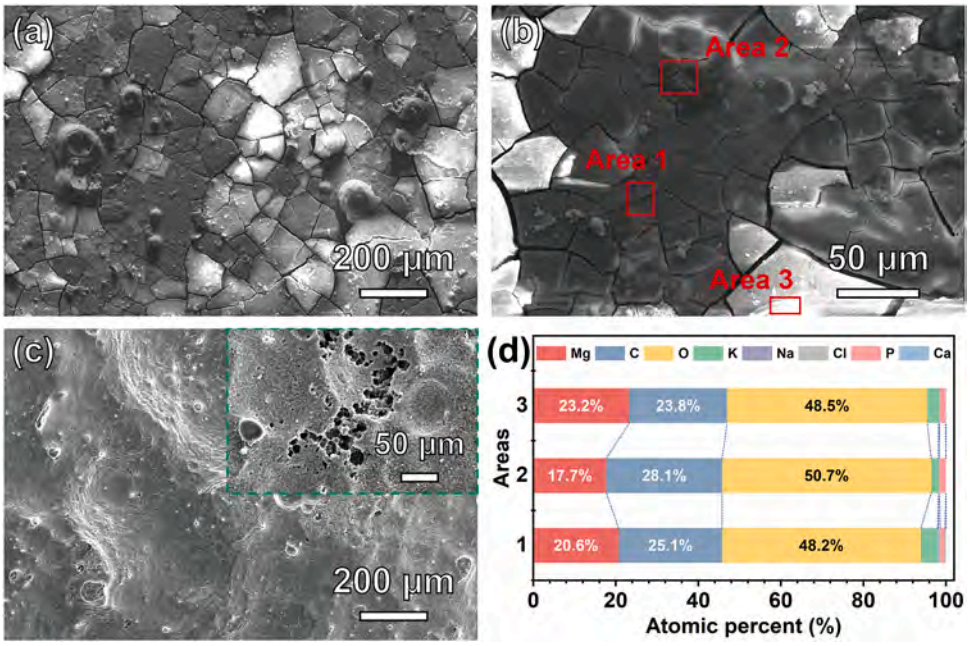

Fig. 10. SEM images of the WE43 alloy: (a, b) Before and (c) After removing the corrosion products and (d) Chemical compositions of the selected areas in (b).

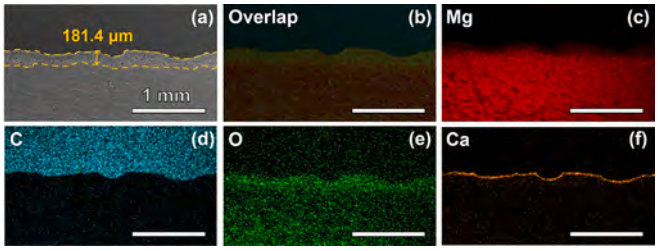

Fig. 11. (a) Cross-section morphology and (b)-(f) EDS maps of the WE43 alloy after degradation.

entanglement between molecular chains decreases and the mobility of the molecular chains in the PLA membrane increases consistent with GPC. Chain scission may occur during immersion contributing to the increased crystallinity. These changes are beneficial to the permeation of water molecules as well as anions and cations in Hanks' solution.

The PLA membrane is prepared by solvent evaporation and so both porous and dense surfaces are observed, as shown in Fig. 8. As a result of the hydrolysis of PLA, large and deep micropores as well as swellings are found from both surfaces. Na, Cl, Mg, and K which are the main aggressive elements in Hanks' solution are detected from both surfaces, especially in the vicinity of micropores. This provides evidence that anions and cations in Hanks' solution and DI water permeate the coating and micropores created by hydrolysis of PLA provide the ion penetration channels. The different elemental distributions on the porous and dense surfaces may be attributed to the different ion permeation behavior of anions and cations.

In general, the difference in the ion concentrations in Hanks' solution and DI water is responsible for the hydrostatic pressure, chemical potential, and concentration gradients [33]. Herein, water molecules, anions and cations first enter the PLA membrane and then diffuse into DI water due to the gradients. However, diffusion through the polymer is a rate limiting step [33]. As illustrated in Fig. 2, the concentrations of Na^+ and Cl^- are larger than the initial concentrations. Specifically, Na^+ increases gradually but Cl^- fluctuates. Cl^- plays a dominant role in the first 348 h but Na^+ makes a large contribution during further immersion. The difference can be explained by the different ion radii of Na^+ and Cl^-. David et al. [41] have reported that the hydrated ion radius depends on the charge and size of the ion. Although Na^+ (0.117 nm) has a smaller radius than Cl^- (0.164 nm), the ion radius of hydrated Na^+ (0.358 nm) is larger than that of hydrated Cl^- (0.332 nm) [33,42,43]. Consequently, Cl^- penetrates more rapidly than Na^+ during initial degradation.

Reaction (4) is generally considered to occur because of the reactive nature of Mg [13,44,45]. In addition, Mg^{2+} may react with -COOH formed by hydrolysis of PLA as shown in Eq. (5) [4,28]:

$$Mg + 2H_2O \rightarrow Mg(OH)_2 + 2H_2. \quad (4)$$

$$Mg^{2+} + 2-COOH \rightarrow (-COO)_2Mg + 2H^+. \quad (5)$$

Degradation of the PLA membrane and change in ion permeation impact corrosion of the WE43 alloy. Based on the ion concentration curves, the degradation process can be divided into three stages since the Cl^- and Na^+ exhibit distinct transitions at time points of 120 h and 348 h. The protection mechanism and corrosion behavior illustrated in Fig. 12 are discussed in the following.

In the first stage (0–120 h), the PLA membrane is a good barrier preventing Na^+ and Cl^- from penetration. The hydrated anions and cations in Hanks' solution may be embedded preferentially in the vicinity of the micropores on the porous surface of PLA. Water molecules adsorb onto the PLA membrane and on account of the absence of anions and cations in this stage, Mg mainly reacts with H_2O, as shown in Eq. (4). Therefore, a double-layer oxide film composed of an inner layer of MgO and outer layer of $Mg(OH)_2$ is formed in this stage.

In the second stage (120–348 h), the PLA membrane is hydrolyzed gradually and as a result of the hydrostatic pressure, chemical potential, and concentration gradients, anions and cations permeate from Hanks' solution to DI water. Compared to Na^+, Cl^- with a smaller hydrated radius and large concentration permeates faster. $Mg(OH)_2$ formed in Stage 1 is porous and cannot block aggressive Cl^-. The infiltration of Cl^- into the $Mg(OH)_2$ leads to the destabilization of the hydroxylated interface [46]. Therefore, R_{ct} decreases between 120 and 216 h, indicating that the corrosion resistance deteriorates. Small corrosion pits are observed but insulation by the PLA membrane limits the Cl^- concentration (< 2.40 mmol/L), so that R_{ct} increases gradually between 216 h and 348 h, implying a thicker $Mg(OH)_2$ layer and enhanced corrosion resistance.

In the third stage (348–504 h), the PLA membrane suffers from

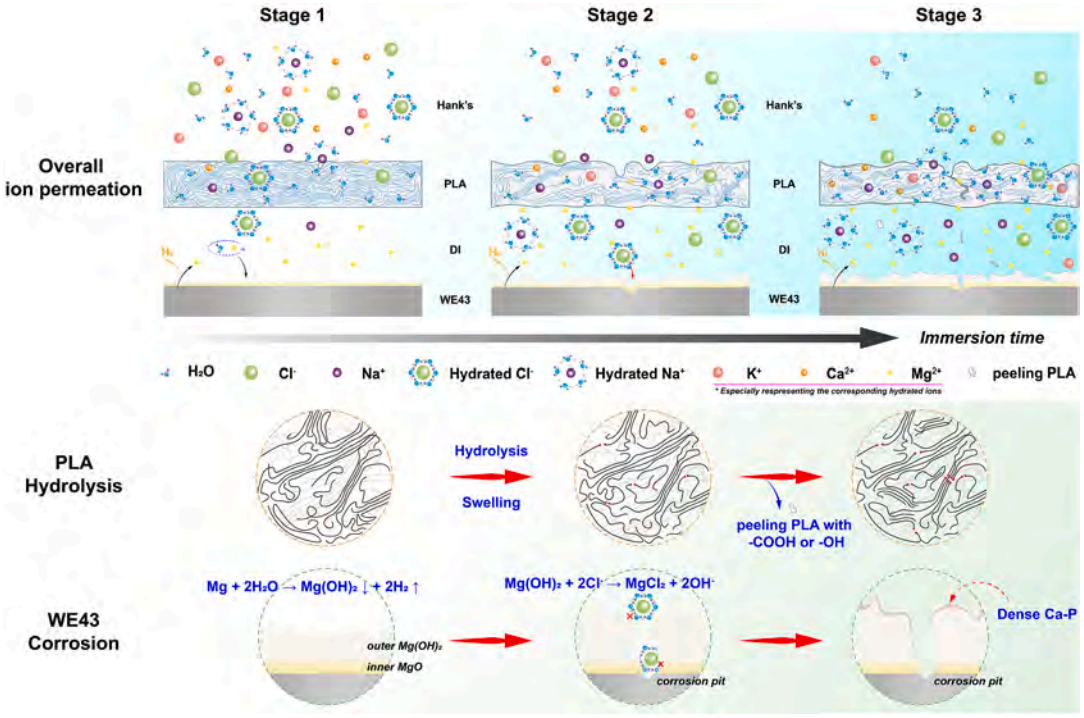

Fig. 12. Schematic illustration of the degradation process.

serious hydrolysis and the pH decreases as shown in Fig. 3. The entangled segments are stretched thereby allowing more water molecules, anions, and cations to penetrate the PLA membrane. Therefore, the concentration of Na^+ with a larger hydrated radius increases. Meanwhile, hydrated K^+, Ca^{2+}, and Mg^{2+} with radii of 0.331 nm, 0.412 nm, and 0.428 nm, respectively [42], also permeate the PLA membrane consequently inhibiting penetration of Cl^-. The hysteretic ions act as a pH buffer in DI water and this may be another reason why the pH decreases. Owing to the presence of Ca^{2+} and relevant anions, denser and more stable Ca−P is deposited on the WE43 alloy to enhance the corrosion resistance as manifested by a slightly larger R_{ct} in this stage.

4.2. Protection rendered by the coating

It is necessary to understand the protection mechanism and changes especially when the biodegradable coating and metallic matrix

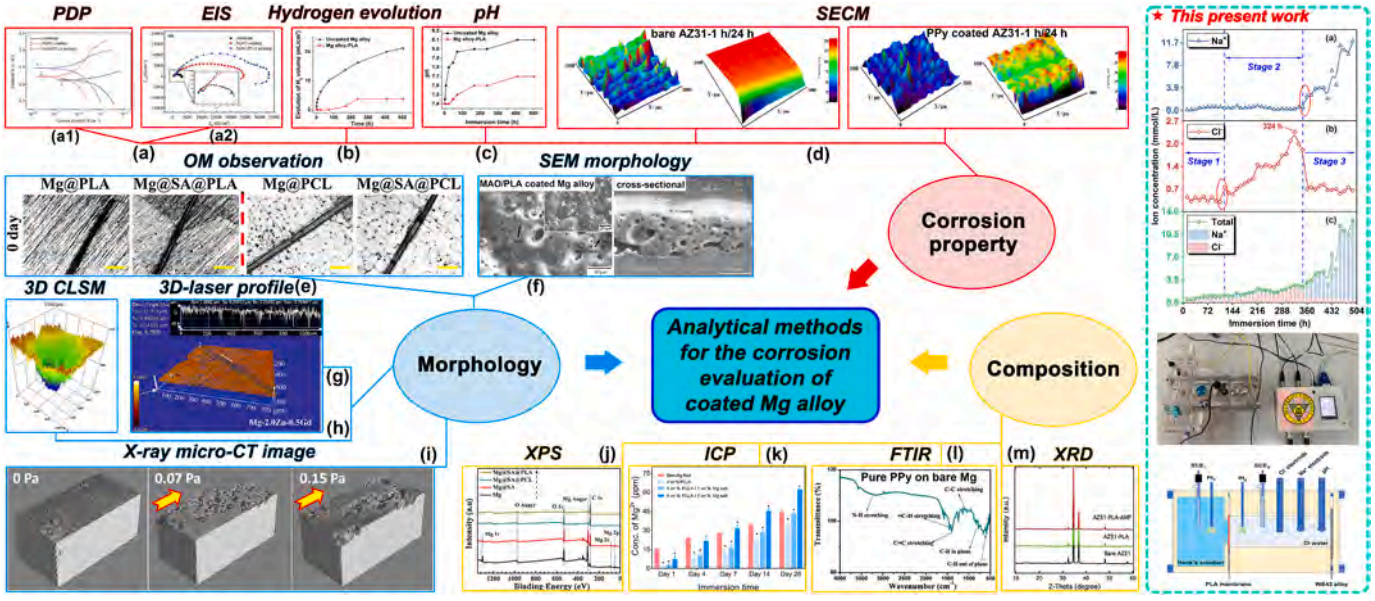

Fig. 13. (a) PDP (a1) and EIS (a2) of the MAO/PLA coated Mg-1.21Li-1.12Ca-1.0Y alloy [16]; (b) Hydrogen evolution; (c) pH change of AZ31 alloy with and without the PLA coating [25]; (d) SECM maps of the AZ31 alloy with and without the PPy coating [54]; (e) OM of the corroded morphologies of Mg with the SA@PLA/SA@PCL coatings [18]; (f) SEM morphology of the corroded MAO/PLA coated Mg-1.21Li-1.12Ca-1.0Y alloy [16]; (g) Local observation of bare Mg-2.0Zn-0.5Gd alloy by 3D-laser profiling [47]; (h) 3D corroded morphology of the bare ZW25 alloy by CLSM [48]; (i) X-ray micro CT results of the bare MgZnCa plate under the flow-induced shear stress [49]; (j) XPS spectra of Mg with the SA@PLA/SA@PCL coatings [18]; (k) ICP of the PLLA/$MgSO_4$·$7H_2O$ coated Mg [50]; (l) FTIR spectrum of pure PPy on the bare AZ31 Mg alloy [54]; (m) XRD patterns of the PLA coated AZ31 alloy [51]. Reproduced based on the cited studies.

complicate the process. It has been reported that the corrosion resistance of PLA coatings on biodegradable Mg alloys changes with time [15,18,23–27]. Permeation of the anions and cations through the PLA coating plays a crucial role in corrosion of the Mg alloy and degradation of PLA and Mg in turn affects the permeation behavior in turn.

At present, the typical analytical methods to evaluate corrosion assess the corrosion properties, morphology, and composition [3,13,16,18,25,47–51] as summarized in Fig. 13. Common methods including PDP, EIS, hydrogen evolution and pH monitoring are used to evaluate the overall corrosion resistance of coated Mg alloys. In general, the morphology and composition of the coating are observed before and after the corrosion test. Among the various methods, SECM can measure the local corrosion density [3], but the current density difference may decrease as the coating becomes thicker. Furthermore, real-time OM observation is limited by the resolution and small differences in the protection mechanism may not be unraveled. Based on previous findings, protection can be monitored by EIS, hydrogen evolution, and corroded surface morphology change, besides studies of the external solution components or degradation product compositions [22,29,30]. Based on the results presented here, SEM and FTIR can also be utilized to monitor the changes in the morphology and functional groups before and after degradation and GPC and DSC are useful in analyzing the variations in the molecular weight, glass transition, melting point, and melting enthalpy [52,53].

Owing to existing limitations, accurate simulation of the microenvironment at the interface between the coating and Mg alloy is important to bridging the gap between theoretical studies and experiments. As discussed in Section 4.1, the hydrolysis of PLA is influenced by water molecules and the penetrating anions and cations. The morphological and structural changes in the PLA membrane reveal the permeation behavior. Owing to the different hydrated ion radii, Na^+ and Cl^- have different permeation rates as shown by the ion concentration curves and EIS. In addition, R_{ct} obtained by the electrochemical test is time dependent as a result of PLA degradation and ion permeation. The important issues are degradation of the PLA membrane, permeation of the anions and cations, and corrosion of the WE43 alloy. Since K and Ca are detected from the degraded PLA and corroded WE43 alloy, the fluid flow conditions and different corrosive media are important factors [55,56] and more research is needed in the future for further clarification.

4.3. Prediction of the protection efficiency

The protection effectiveness rendered by the coating is related to ion permeation which is time dependent. Herein, ion permeation is investigated with the aid of the ion concentration curves and $R_{s\text{-}DI}$ obtained by EIS. Fick's second law is utilized to calculate the diffusion coefficients of Na^+ and Cl^- as shown in the following:

$$\frac{C_s - C_x}{C_s - C_0} = erf\left(\frac{x}{\sqrt{4Dt}}\right). \quad (6)$$

where Cs is the ion concentration in Hanks' solution, C_x is the ion concentration at a distance x, C_0 is the initial ion concentration in DI water, x is the distance, D is the diffusion coefficient, t is the degradation time, and x represents the thickness of the PLA membrane. D_{Cl^-} and D_{Na^+} were derived and as shown in Fig. 14(a), a small difference is observed from the diffusion coefficients of Na^+ and Cl^-. The relationship of D_{Cl^-} and D_{Na^+} *versus* degradation time is represented by the following equations:

$$D_{Cl^-} = 8.225 \times 10^{-9} \times t^{-0.990}. \quad (7)$$

$$D_{Na^+} = 8.000 \times 10^{-9} \times t^{-0.929}. \quad (8)$$

To better reflect the difference between D_{Cl^-} and D_{Na^+}, ΔD is calculated by Eq. (9):

$$\Delta D = D_{Cl^-} - D_{Na^+}. \quad (9)$$

According to the diffusion coefficient difference of Na^+ and Cl^-, Cl^- plays a dominant role in the first 348 h but Na^+ dominates thereafter consistent with Fig. 2.

$R_{s\text{-}DI}$ is derived by EIS and Fig. 14(b) presents the relationship between $R_{s\text{-}DI}$ and immersion time. Since the conductivity exhibits a reciprocal relationship with $R_{s\text{-}DI}$, it can be inferred that the conductivity increases gradually with immersion time. Variation of $R_{s\text{-}DI}$ is similar to that of the diffusion coefficients and the change of $R_{s\text{-}DI}$ with degradation time can be expressed as follows:

$$R_{s-DI} = 3395.85 \times t^{-0.555}. \quad (10)$$

Eqs. (7), (8), and (10) can be used to describe the ion permeation behavior with time and also predict the protection effectiveness of the PLA coating. Moreover, Eq. (7) and Eq. (8) can be incorporated into Eq. (6) to derive the ion concentration at a certain time. However, the failure time calculated by Eq. (10) seems to be shorter than that by Eq. (7) and Eq. (8). This can be explained by that the $R_{s\text{-}DI}$ variation is caused by all the penetrating ions, but the diffusion coefficients only account for individual species.

In general, the various permeation behaviors through the PLA membrane are quantitatively obtained for the typical Na^+ and Cl^- in Hanks' solution. In addition, the diffusion of Na^+ and Cl^- can be predicted according to the numerical models established herein. Combined with the ion permeation and the PLA degradation, the corrosion protection mechanism of the PLA coatings has been better clarified in this work, which may enrich our understanding of the polymeric coated Mg-based biomedical implants. Specifically, Ca^{2+}, PO_4^{3-} along with other cations and anions take part in the third stage leading to the formation of Ca−P on the WE43 substrate. Therefore, the deposition of Ca−P could

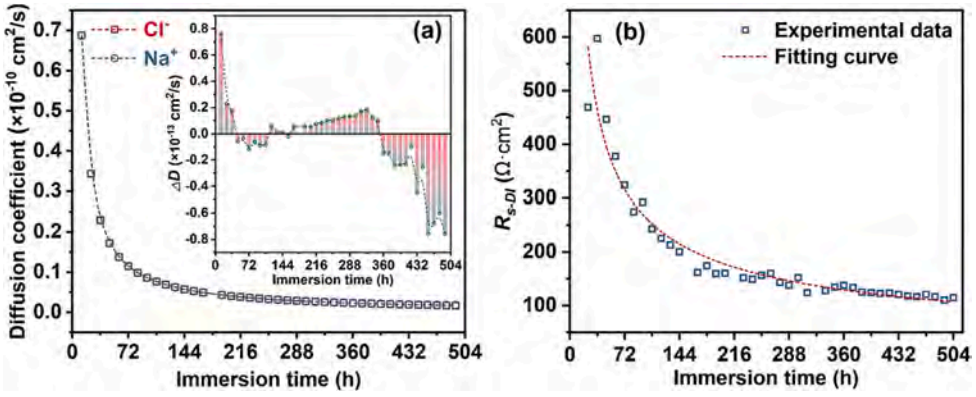

Fig. 14. (a) Diffusion coefficients of Na^+ and Cl^- during the degradation process as well as the relationship of ΔD *versus* immersion time and (b) $R_{s\text{-}DI}$ *versus* immersion time.

be regulated by controlling the selective permeation of the specific ions. And this may be dependent on the introduction of the environment at the interface and the design of the polymeric coating itself, including degradability, crystallinity, chargeability, and self-healing properties.

5. Conclusions

The protection behavior and mechanism of the WE43 Mg alloy coated with poly-lactic acid are investigated and the following conclusions can be drawn.

(1) Ion permeation can be divided into three stages. Specifically, Cl^- plays a dominant role in the first 348 h during immersion and Na^+ dominates thereafter.
(2) Penetration of Ca^{2+}, PO_4^{3-} along with other ions take part in the third stage leading to the formation of Ca−P on the WE43 substrate.
(3) The corrosion resistance of WE43 alloy improves because the PLA membrane inhibits ion penetration. The corrosion resistance changes with time because of the combined effects of PLA degradation and ion permeation.
(4) According to Fick's second law, a model is proposed to describe the ion permeation phenomenon. In addition, a numerical model is formulated based on the fitted EIS data. By using the two models, the protection effectiveness of the PLA coating can be analyzed and predicted. They are very helpful in enriching our understanding of the protection behavior and mechanism of polymeric coatings on Mg alloys.

CRediT authorship contribution statement

Jianwei Dai: Conceptualization, Methodology, Investigation, Writing – original draft, Writing – review & editing. **Changqing Wu:** Methodology, Investigation. **Juyi Yang:** Methodology, Investigation. **Lu Zhang:** Formal analysis, Validation. **Qiangsheng Dong:** Methodology. **Linyuan Han:** Investigation. **Xuan Li:** Conceptualization, Methodology, Writing – review & editing. **Jing Bai:** Resources, Investigation. **Feng Xue:** Resources, Investigation. **Paul K. Chu:** Writing – review & editing. **Chenglin Chu:** Supervision, Funding acquisition, Visualization, Writing – review & editing.

Declaration of competing interest

The authors declare that they have no known competing financial interests or personal relationships that could have appeared to influence the work reported in this paper.

Data availability

All data generated or analyzed during this study are available from the corresponding author upon reasonable request.

Acknowledgements

This research was supported by the National Natural Science Foundation of China (Grant No. 52171236), the Open Research Fund of Jiangsu Key Laboratory for Advanced Metallic Materials (Grant No. AMM2021A01), Postgraduate Research & Practice Innovation Program of Jiangsu Province (Grant No. KYCX20_0091), City University of Hong Kong Donation Research Grant (Grant No. DON-RMG 9229021), Hong Kong PDFS - RGC Postdoctoral Fellowship Scheme (Grant No. PDFS2122-1S08 and CityU 9061014), and Hong Kong HMRF (Health and Medical Research Fund) (Grant No. 2120972 and CityU 9211320).

The authors also would like to thank Nanjing Jingmai Technology Co., Ltd. for their suggestion and assistance in the fabrication of the *in-situ* apparatus to study the ion permeation behavior.

References

[1] Y.F. Zheng, X.N. Gu, F. Witte, Biodegradable metals, Mater. Sci. Eng. R-Rep. 77 (2014) 1–34.
[2] Q.S. Dong, J.W. Dai, K. Qian, H. Liu, X.X. Zhou, Q.Q. Yao, M.M. Lu, C.L. Chu, F. Xue, J. Bai, Dual self-healing inorganic-organic hybrid coating on biomedical Mg, Corros. Sci. 200 (2022), 110230.
[3] X. Li, Y. Wang, C.L. Chu, L.Y. Han, J. Bai, F. Xue, A study on Mg wires/poly-lactic acid composite degradation under dynamic compression and bending load for implant applications, J. Mech. Behav. Biomed. Mater. 105 (2020), 103707.
[4] H. Cai, J. Meng, X. Li, F. Xue, C.L. Chu, C. Guo, J. Bai, In vitro degradation behavior of Mg wire/poly(lactic acid) composite rods prepared by hot pressing and hot drawing, Acta Biomater. 98 (2019) 125–141.
[5] Y.J. Chen, Z.G. Xu, C. Smith, J. Sankar, Recent advances on the development of magnesium alloys for biodegradable implants, Acta Biomater. 10 (2014) 4561–4573.
[6] Y. Liu, Y.F. Zheng, X.H. Chen, J.A. Yang, H.B. Pan, D.F. Chen, L.N. Wang, J. L. Zhang, D.H. Zhu, S.L. Wu, K.W.K. Yeung, R.C. Zeng, Y. Han, S.K. Guan, Fundamental theory of biodegradable metals—definition, criteria, and design, Adv. Funct. Mater. 29 (2019), 1805402.
[7] C. Rendenbach, H. Fischer, A. Kopp, K. Schmidt-Bleek, H. Kreiker, S. Stumpp, M. Thiele, G. Duda, H. Hanken, B. Beck-Broichsitter, O. Jung, N. Kroger, R. Smeets, M. Heiland, Improved in vivo osseointegration and degradation behavior of PEO surface-modified WE43 magnesium plates and screws after 6 and 12 months, Mater. Sci. Eng. C-Mater. Biol. Appl. 129 (2021), 112380.
[8] E. Marukawa, M. Tamai, Y. Takahashi, I. Hatakeyama, M. Sato, Y. Higuchi, H. Kakidachi, H. Taniguchi, T. Sakamoto, J. Honda, K. Omura, H. Harada, Comparison of magnesium alloys and poly-l-lactide screws as degradable implants in a canine fracture model, J. Biomed. Mater. Res. Part B 104 (2016) 1282–1289.
[9] S. Hiromoto, S. Itoh, K. Doi, H. Katayama, T. Akashi, Short- and long-term corrosion behavior of carbonate apatite-coated mg-4mass% Y-3mass% RE alloy in cell culture medium, Corros. Sci. 200 (2022), 110222.
[10] L.Y. Li, L.Y. Cui, R.C. Zeng, S.Q. Li, X.B. Chen, Y. Zheng, M.B. Kannan, Advances in functionalized polymer coatings on biodegradable magnesium alloys - a review, Acta Biomater. 79 (2018) 23–36.
[11] Y.W. Zhu, W. Liu, T. Ngai, Polymer coatings on magnesium-based implants for orthopedic applications, J. Polym. Sci. 60 (2021) 32–51.
[12] N. Singh, U. Batra, K. Kumar, N. Ahuja, A. Mahapatro, Progress in bioactive surface coatings on biodegradable Mg alloys: A critical review towards clinical translation, Bioact. Mater. 19 (2023) 717–757.
[13] M. Esmaily, J.E. Svensson, S. Fajardo, N. Birbilis, G.S. Frankel, S. Virtanen, R. Arrabal, S. Thomas, L.G. Johansson, Fundamentals and advances in magnesium alloy corrosion, Prog. Mater. Sci. 89 (2017) 92–193.
[14] T. Casalini, F. Rossi, A. Castrovinci, G. Perale, A perspective on polylactic acid-based polymers use for nanoparticles synthesis and applications, Front. Bioeng. Biotechnol. 7 (2019) 259.
[15] H.M. Mousa, A. Abdal-Hay, M. Bartnikowski, I.M.A. Mohamed, A.S. Yasin, S. Ivanovski, C.H. Park, C.S. Kim, A multifunctional zinc Oxide/Poly(Lactic Acid) nanocomposite layer coated on magnesium alloys for controlled degradation and antibacterial function, ACS Biomater. Sci. Eng. 4 (2018) 2169–2180.
[16] R.C. Zeng, W.C. Qi, Y.W. Song, Q.K. He, H.Z. Cui, E.H. Han, In vitro degradation of MAO/PLA coating on Mg-1.21Li-1.12Ca-1.0Y alloy, Front. Mater. Sci. 8 (2014) 343–353.
[17] H.R. Bakhsheshi-Rad, E. Hamzah, R. Ebrahimi-Kahrizsangi, M. Daroonparvar, M. Medraj, Fabrication and characterization of hydrophobic microarc oxidation/poly-lactic acid duplex coating on biodegradable Mg–Ca alloy for corrosion protection, Vacuum 125 (2016) 185–188.
[18] W.T. Zhang, Y.Q. Chen, M.Y. Chen, S. Zhao, J.L. Mao, A. Qu, W. Li, Y.C. Zhao, N. Huang, G.J. Wan, Strengthened corrosion control of poly (lactic acid) (PLA) and poly (ε-caprolactone) (PCL) polymer-coated magnesium by imbedded hydrophobic stearic acid (SA) thin layer, Corros. Sci. 112 (2016) 327–337.
[19] M.M. Alrashed, S. Jana, M.D. Soucek, Corrosion performance of polyurethane hybrid coatings with encapsulated inhibitor, Prog. Org. Coat. 130 (2019) 235–243.
[20] H. Cai, F. Xue, C.L. Chu, J. Bai, H.X. Wang, D. Zhu, X. Li, B. Han, W.T. Gao, Z. S. Hang, Internal morphology evolution of mg Wire/Poly(Lactic Acid) composites during degradation process characterized by X-ray computed tomography, J. Mater. Eng. Perform. 31 (2022) 4507–4518.
[21] M. Ebrahimifar, M. Taherimehr, Evaluation of in-vitro drug release of polyvinylcyclohexane carbonate as a CO_2-derived degradable polymer blended with PLA and PCL as drug carriers, J. Drug Deliv. Sci. Technol. 63 (2021), 102491.
[22] B. Tyler, D. Gullotti, A. Mangraviti, T. Utsuki, H. Brem, Polylactic acid (PLA) controlled delivery carriers for biomedical applications, Adv. Drug Deliv. Rev. 107 (2016) 163–175.
[23] X. Sun, Q.S. Yao, Y.C. Li, F. Zhang, R.C. Zeng, Y.H. Zou, S.Q. Li, Biocorrosion resistance and biocompatibility of Mg-Al layered double hydroxide/poly(L-lactic acid) hybrid coating on magnesium alloy AZ31, Front. Mater. Sci. 14 (2020) 426–441.
[24] A. Ferrandez-Montero, M. Lieblich, J.L. Gonzalez-Carrasco, R. Benavente, V. Lorenzo, R. Detsch, A.R. Boccaccini, B. Ferrari, Development of biocompatible and fully bioabsorbable PLA/Mg films for tissue regeneration applications, Acta Biomater. 98 (2019) 114–124.
[25] M.E. Voicu, I. Demetrescu, A. Dorobantu, M. Enachescu, G.O. Buica, D. Ionita, Interaction of mg alloy with PLA electrospun nanofibers coating in understanding changes of corrosion, wettability, and pH, Nanomaterials 12 (2022) 1369.

[26] M. Muñoz, B. Torres, M. Mohedano, E. Matykina, R. Arrabal, A.J. López, J. Rams, PLA deposition on surface treated magnesium alloy: Adhesion, toughness and corrosion behaviour, Surf. Coat. Technol. 388 (2020), 125593.
[27] A. Alabbasi, S. Liyanaarachchi, M.B. Kannan, Polylactic acid coating on a biodegradable magnesium alloy: An in vitro degradation study by electrochemical impedance spectroscopy, Thin Solid Films 520 (2012) 6841–6844.
[28] X. Li, C.L. Chu, Y.L. Wei, C.X. Qi, J. Bai, C. Guo, F. Xue, P.H. Lin, P.K. Chu, *In vitro* degradation kinetics of pure PLA and Mg/PLA composite: Effects of immersion temperature and compression stress, Acta Biomater. 48 (2017) 468–478.
[29] I. Grizzi, H. Garreau, S. Li, M. Vert, Hydrolytic degradation of devices based on poly(DL-lactic acid) size-dependence, Biomater. 16 (1995) 305–311.
[30] S.Y. Du, Y. Zhang, M.J. Meng, A. Tang, Y. Li, The role of water transport in the failure of silicone rubber coating for implantable electronic devices, Prog. Org. Coat. 159 (2021), 106419.
[31] X. Li, X.M. Liu, S.L. Wu, K.W.K. Yeung, Y.F. Zheng, P.K. Chu, Design of magnesium alloys with controllable degradation for biomedical implants: From bulk to surface, Acta Biomater. 45 (2016) 2–30.
[32] R.N. Oosterbeek, C.K. Seal, J.-M. Seitz, M.M. Hyland, Polymer–bioceramic composite coatings on magnesium for biomaterial applications, Surf. Coat. Technol. 236 (2013) 420–428.
[33] G.M. Geise, D.R. Paul, B.D. Freeman, Fundamental water and salt transport properties of polymeric materials, Prog. Polym. Sci. 39 (2014) 1–42.
[34] X.M. Su, Q. Zhou, Q.Y. Zhang, Y. Zhang, H. Zhang, Study on the deterioration process of bipolar coating using electrochemical impedance spectroscopy, Appl. Surf. Sci. 257 (2011) 6095–6101.
[35] Y.H. Dong, Q. Zhou, Relationship between ion transport and the failure behavior of epoxy resin coatings, Corros. Sci. 78 (2014) 22–28.
[36] S.Q. Liu, G.H. Wu, X.G. Chen, X.F. Zhang, J.J. Yu, M.F. Liu, Y. Zhang, P. Wang, Degradation behavior in vitro of carbon nanotubes (CNTs)/Poly(lactic acid) (PLA) composite suture, Polymers 11 (2019) 1015.
[37] E. Barsoukov, J.R. Macdonald, Impedance Spectroscopy, 2018.
[38] D. Sotta, J. Bernard, V. Sauvant-Moynot, Application of electrochemical impedance spectroscopy to the study of ionic transport in polymer-based electrolytes, Prog. Org. Coat. 69 (2010) 207–214.
[39] G.J. Brug, A.L.G. van den Eeden, M. Sluyters-Rehbach, J.H. Sluyters, The analysis of electrode impedances complicated by the presence of a constant phase element, J. Electroanal. Chem. 176 (1984) 275–295.
[40] Z.X. Chen, D. Ding, T. Yu, W.D. Yang, Q. Li, Y. Li, Enzymatic degradation behaviors and kinetics of bio-degradable jute/poly (lactic acid) (PLA) composites, Compos. Commun. 33 (2022), 101227.
[41] F. David, V. Vokhmin, G. Ionova, Water characteristics depend on the ionic environment. Thermodynamics and modelisation of the aquo ions, J. Mol. Liq. 90 (2001) 45–62.
[42] A.G. Volkov, S. Paula, D.W. Deamer, Two mechanisms of permeation of small neutral molecules and hydrated ions across phospholipid bilayers, Bioelectrochem. Bioenerg. 42 (1997) 153–160.
[43] S.G. Croll, Electrolyte transport in polymer barrier coatings: perspectives from other disciplines, Prog. Org. Coat. 124 (2018) 41–48.
[44] K. Chen, J.W. Dai, X.B. Zhang, Improvement of corrosion resistance of magnesium alloys for biomedical applications, Corros. Rev. 33 (2015) 101–117.
[45] A. Atrens, S. Johnston, Z. Shi, M.S. Dargusch, Viewpoint - Understanding Mg corrosion in the body for biodegradable medical implants, Scr. Mater. 154 (2018) 92–100.
[46] I. Giner, O. Ozcan, G. Grundmeier, In situ AFM studies of the stability of MgO(1 0 0) in aqueous electrolytes, Corros. Sci. 87 (2014) 51–59.
[47] H.W. Miao, D.D. Zhang, C.X. Chen, L. Zhang, J. Pei, Y. Su, H. Huang, Z.C. Wang, B. Kang, W.J. Ding, H. Zeng, G.Y. Yuan, Research on biodegradable Mg–Zn–Gd alloys for potential orthopedic implants: In vitro and in vivo evaluations, ACS Biomater. Sci. Eng. 5 (2019) 1623–1634.
[48] C.Q. Li, D.K. Xu, Z.R. Zeng, B.J. Wang, L.Y. Sheng, X.B. Chen, E.H. Han, Effect of volume fraction of LPSO phases on corrosion and mechanical properties of Mg-Zn-Y alloys, Mater. Des. 121 (2017) 430–441.
[49] J. Wang, V. Giridharan, V. Shanov, Z.G. Xu, B. Collins, L. White, Y. Jang, J. Sankar, N. Huang, Y. Yun, Flow-induced corrosion behavior of absorbable magnesium-based stents, Acta Biomater. 10 (2014) 5213–5223.
[50] Y.W. Zhu, L.Z. Zheng, W. Liu, L. Qin, T. Ngai, Poly(l-lactic acid) (PLLA)/$MgSO_4{\cdot}7H_2O$ composite coating on magnesium substrates for corrosion protection and cytocompatibility promotion, ACS Appl. Bio Mater. 3 (2020) 1364–1373.
[51] Y.F. Ren, E. Babaie, S.B. Bhaduri, Nanostructured amorphous magnesium phosphate/poly (lactic acid) composite coating for enhanced corrosion resistance and bioactivity of biodegradable AZ31 magnesium alloy, Prog. Org. Coat. 118 (2018) 1–8.
[52] M. Karimi-Avargani, F. Bazooyar, D. Biria, A. Zamani, M. Skrifvars, The special effect of the *Aspergillus flavus* and its enzymes on biological degradation of the intact polylactic acid (PLA) and PLA-Jute composite, Polym. Degrad. Stab. 179 (2020), 109295.
[53] S. Farah, D.G. Anderson, R. Langer, Physical and mechanical properties of PLA, and their functions in widespread applications - A comprehensive review, Adv. Drug Deliv. Rev. 107 (2016) 367–392.
[54] V. Jothi, A.Y. Adesina, A.M. Kumar, M.M. Rahman, J.S.N. Ram, Enhancing the biodegradability and surface protective performance of AZ31 Mg alloy using polypyrrole/gelatin composite coatings with anodized Mg surface, Surf. Coat. Technol. 381 (2020), 125139.
[55] K. Chen, X.N. Gu, H. Sun, H.Y. Tang, H.T. Yang, X.H. Gong, Y.B. Fan, Fluid-induced corrosion behavior of degradable zinc for stent application, J. Mater. Sci. Technol. 91 (2021) 134–147.
[56] D. Mei, S.V. Lamaka, X.P. Lu, M.L. Zheludkevich, Selecting medium for corrosion testing of bioabsorbable magnesium and other metals – A critical review, Corros. Sci. 171 (2020), 108722.